

Originally published as:

Xiong, C., Lühr, H., Yamazaki, Y. (2019): An Opposite Response of the Low-Latitude Ionosphere at Asian and American Sectors During Storm Recovery Phases: Drivers From Below or Above. - *Journal of Geophysical Research*, 124, 7, pp. 6266—6280.

DOI: <http://doi.org/10.1029/2019JA026917>

# JGR Space Physics

## RESEARCH ARTICLE

10.1029/2019JA026917

### Key Points:

- The dayside low-latitude ionosphere on 9–11 September 2017 exhibits prominent positive/negative responses at the Asian/American sectors
- The global distribution of thermospheric O/N<sub>2</sub> ratio measured by GUVI cannot well explain such longitudinal opposite response of ionosphere
- We suggest lower atmospheric forcing the main contributor to the longitudinal opposite response of ionosphere on 9–11 September 2017

### Correspondence to:

C. Xiong,  
bear@gfz-potsdam.de

### Citation:

Xiong, C., Lühr, H., & Yamazaki, Y. (2019). An opposite response of the low-latitude ionosphere at Asian and American sectors during storm recovery phases: Drivers from below or above. *Journal of Geophysical Research: Space Physics*, 124, 6266–6280. <https://doi.org/10.1029/2019JA026917>



Received 3 MAY 2019

Accepted 30 JUN 2019

Accepted article online 15 JUL 2019

Published online 23 JUL 2019

## An Opposite Response of the Low-Latitude Ionosphere at Asian and American Sectors During Storm Recovery Phases: Drivers From Below or Above

Chao Xiong<sup>1</sup> , Hermann Lühr<sup>1</sup> , and Yosuke Yamazaki<sup>1</sup>
<sup>1</sup>GFZ German Research Centre for Geosciences, Potsdam, Germany

**Abstract** In this study, we focus on the recovery phase of a geomagnetic storm that happened on 6–11 September 2017. The ground-based total electron content data, as well as the *F* region in situ electron density, measured by the Swarm satellites show an interesting feature, revealing at low and equatorial latitudes on the dayside ionosphere prominent positive and negative responses at the Asian and American longitudinal sectors, respectively. The global distribution of thermospheric O/N<sub>2</sub> ratio measured by global ultraviolet imager on board the Thermosphere, Ionosphere, Mesosphere Energetics and Dynamics satellite cannot well explain such longitudinally opposite response of the ionosphere. Comparison between the equatorial electrojet variations from stations at Huancayo in Peru and Davao in the Philippines suggests that the longitudinally opposite ionospheric response should be closely associated with the interplay of *E* region electrodynamics. By further applying nonmigrating tidal analysis to the ground-based total electron content data, we find that the diurnal tidal components, D0 and DW2, as well as the semidiurnal component SW1, are clearly enhanced over prestorm days and persist into the early recovery phase, indicating the possibility of lower atmospheric forcing contributing to the longitudinally opposite response of the ionosphere on 9–11 September 2017.

### 1. Introduction

A geomagnetic storm refers to the temporary disturbances of the near-Earth space environment, caused by the interaction between solar wind/interplanetary magnetic field (IMF) and the Earth's magnetic field. The disturbances that drive geomagnetic storms can be an interplanetary coronal mass ejection or a corotating interaction region-dominated solar wind, originating from a region of weak magnetic field on the Sun's surface (Gonzalez et al., 1994). During geomagnetic storms, in particular, during times of southward IMF, large amounts of energy and momentum are deposited by the disturbed solar wind into the Earth's ionosphere-thermosphere at auroral latitudes. The most rapid reaction is the enhanced plasma convection in the high-latitude ionosphere. Fast antisunward (sunward) plasma flows over the polar cap (at auroral latitudes) drive neutral winds via ion-neutral collisions and set up a large-scale dawn-to-dusk ionospheric electric field (Zhou et al., 2016). The transient high-latitude electric fields can expand almost instantaneously to the equatorial region, which is known as the prompt penetration electric fields (PPEFs; e.g., Nishida, 1968; Kikuchi et al., 1996; Kelley et al., 2003). Additionally, enhanced Joule heating at auroral latitudes causes sudden uplifts of neutral air and launches traveling atmospheric disturbances/traveling ionospheric disturbances and drives equatorward neutral winds (e.g., Hocke & Schlegel, 1996; Huang et al., 2012; Richmond & Matsushita, 1975; Xiong et al., 2015). The equatorward winds turn westward at middle and low latitudes due to the Coriolis force and further generate disturbance dynamo electric fields (DDEFs; e.g., Blanc & Richmond, 1980; Scherliess & Fejer, 1997).

The ionospheric storm is generally a global phenomenon, but strong spatial and local time (LT) dependencies are reported from both model and observational results. Due to seasonal effects, the positive ionospheric storm is more often found in the winter hemisphere, while the negative response prefers to be observed in the summer hemisphere (e.g., Goncharenko et al., 2007; Prölss, 1995). The summer-winter hemispheric asymmetry of ionospheric responses shows also dependences on altitude. Astafyeva et al. (2015) investigated a moderate storm that happened on 29–31 August 2004. They found the enhancement of ground-based total electron content (TEC) and *F*2 peak density, *NmF*2, to be more prominent in the Southern (winter) Hemisphere, while the ionospheric topside measurements show stronger positive response in the Northern (summer) Hemisphere. Prölss (1993) and Fuller-Rowell et al. (1997) pointed out that the storm

surges tend to develop in the night sector, where neutral winds are preferably equatorward and in the longitudinal sector containing the magnetic pole. Therefore, larger ionospheric responses prefer to be observed at longitudes on the nightside where the high-latitude energy injection happens. Fejer et al. (2008) found the prompt penetration vertical drift to be upward/downward during the daytime/nighttime with strong LT dependence at all seasons, with largest evening downward/upward disturbance drifts in the Eastern/Western Hemispheres. Thermospheric neutral winds (Emmert et al., 2004) and vertical plasma drifts (Xiong et al., 2016) show also most prominent disturbances at early morning hours during geomagnetic active periods.

The ionospheric response can be quite different at different storm phases. For example, Yue et al. (2016) investigated the storm on 17–18 March 2013, and they found a positive ionospheric response during the initial and main phases while a negative storm effect during the recovery phase. In addition, over the Asian sector they found a long-lasting (>17 hr) daytime negative storm effect only in the southern hemisphere that was caused by the north-south asymmetry of thermospheric O/N<sub>2</sub> depletion. In another storm that happened on 7–8 September 2017, Lei et al. (2018) reported that the daytime TEC in the Asian sector exhibited a long-lasting enhancement during the storm recovery phase on 9–11 September 2017. They suggested that the TEC enhancement is possibly related to the lower atmospheric forcing during the storm recovery phase. Pedatella and Liu (2018) also argued that it is necessary to include the effects of lower atmosphere variability in order to accurately capture the short-time scale variations of the upper atmospheric response to a geomagnetic storm, for example, the day-to-day variability. Xiong et al. (2016) found that the penetration electric field at low-latitude regions is less dependent on longitude at both the dayside and nightside, while the disturbance zonal wind shows clear longitudinal difference at 00:00–06:00 magnetic local times (MLTs), for example, with much stronger westward wind in 45–135°E longitude. The result also implies that there might be a longitudinal dependence of the ionospheric disturbance dynamo at low-latitude regions. Meanwhile, the lower atmospheric forcing, for example, by nonmigrating tides, can cause also significant longitudinal variability of the ionosphere. That means, at storm periods, especially during the recovery phase, ionospheric variations with longitude, due to lower atmospheric forcing, can be misinterpreted as storm effects.

In this study we focus on the recovery phase of the geomagnetic storm on 9–11 September 2017, during which the daytime TEC exhibits a prominent enhancement and a reduction at the Asian and American longitudes, respectively. By checking observations from multi-instruments, we suggest that such a longitudinally opposite response of the ionosphere at storm recovery phase may be not directly caused by the geomagnetic storm, but more likely reflect the influence of tidal forcing from the lower atmosphere. In the following we first describe the data set in section 2 and then provide observational results in section 3. Comparisons with previous results are then discussed in section 4, and a summary is provided at last in section 5.

## 2. Data Set

### 2.1. Ground-Based TEC and EEJ Measurements

For checking the longitudinal variability of the ionosphere, TEC measurements derived from the worldwide Global Navigation Satellite Systems stations are used in this study, which are freely accessible at the Madrigal database with a time cadence of 5 min (e.g., Coster et al., 2003).

In addition, the variations of the equatorial electrojet (EEJ) intensity have been evaluated using ground-based magnetometer data. The proxy for the EEJ intensity can be obtained by taking the difference in the horizontal (H) component magnetic field perturbations observed at an equatorial station, which is under the direct influence of the EEJ, and at a low-latitude station, which is outside the EEJ belt (e.g., Soares et al., 2018). The EEJ proxy has been derived for the American sector using the magnetic field measurements at Huancayo (12.06°S, 75.33°W) in Peru and Villa Remedios (16.77°S, 68.17°W) in Bolivia. The quasi-dipole latitudes are 0.27°S at Huancayo and 5.67°S at Villa Remedios. Similarly, the EEJ proxy for the East Asian sector has been derived using the magnetometer data from Davao (7.10°N, 125.60°E, quasi-dipole latitude: 0.24°S) and Manila (14.60°N, 120.90°E, quasi-dipole latitude: 7.8°N) on the Philippines, which belong to the African Meridian B-field Education and Research (AMBER) magnetometer network (Yizengaw & Moldwin, 2009).

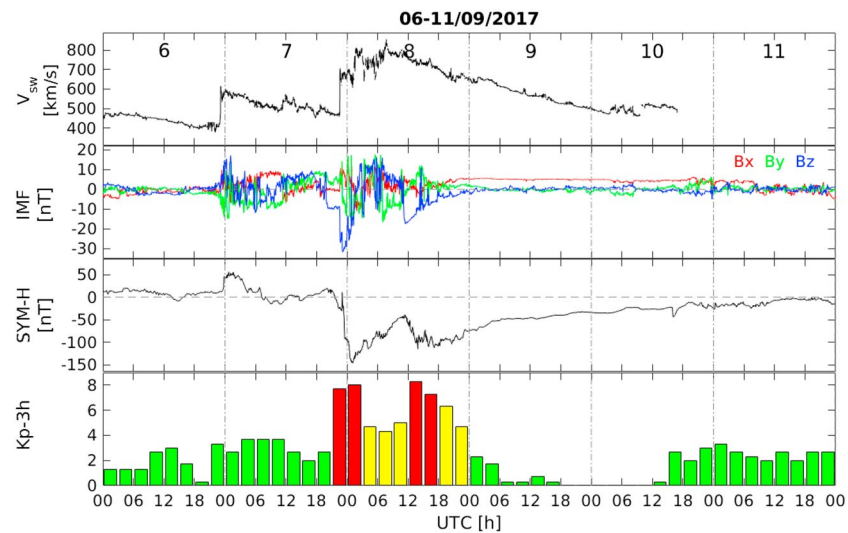


**Figure 1.** The variations of solar wind velocity, IMF components,  $Sym-H$  index, and 3-hr  $Kp$  index on 6–11 September 2017. IMF = interplanetary magnetic field.

## 2.2. In Situ Measurements From Swarm and GUVI

European Space Agency's Swarm constellation is composed of three identical satellites, which was launched on 22 November 2013 into a near-polar orbit ( $87.5^\circ$  inclination) with initial altitude of about 500 km. The final constellation comprising the lower pair, Swarm A and C, is flying side-by-side at an altitude of about 450 km with a longitudinal separation of  $1.4^\circ$  (about 150 km), and the third spacecraft, Swarm B, orbits the Earth at about 510 km at a slightly higher inclination. For covering all 24 hr of LT, Swarm A and C need about 133 days, and Swarm B needs about 141 days. The plasma density is provided by the onboard Langmuir Probe at a sample rate of 2 Hz.

In addition, the thermospheric  $O/N_2$  ratio estimated from the global ultraviolet imager (GUVI) instrument on board the Thermosphere, Ionosphere, Mesosphere Energetics and Dynamics (TIMED) satellite (Christensen et al., 2003) has also been analyzed in this study. The TIMED satellite was launched in December 2001 into an altitude of 625 km with an inclination of  $74.1^\circ$ . The slow orbital precession makes full LT coverage within 2 months. The GUVI instrument observes thermospheric far ultraviolet airglow across the Earth's limb and disk in five spectral channels: HI 121.6 nm, OI 130.4 nm, OI 135.6 nm,  $N_2$  LBHS (141.0–152.8 nm), and  $N_2$  LBH long (167.2–181.2 nm). The  $O/N_2$  ratio from GUVI is derived from the ratio of OI 135.6 nm and LBHS radiances that represent the integration of the product of the volume emission rate and the transmission to the observer throughout the column line of sight. More detailed information about GUVI/TIMED measurements can be found in Christensen et al. (2003, and references therein).

## 3. Ionospheric Response During the Storm on 6–11 September 2017

### 3.1. Overview of the Geomagnetically Disturbed Conditions

During 6–11 September 2017, a spate of solar activity was observed. The Sun released dozens of M-class and four X-class flares, as well as several powerful interplanetary coronal mass ejections that cause near-Earth environment disturbances during this period. From top to bottom, Figure 1 presents the variations of solar wind velocity ( $V_{sw}$ ), three components of IMF in geocentric-solar-magnetospheric coordinates, geomagnetic indices  $Sym-H$ , and the 3-hr  $Kp$  during 6–11 September 2017. Two abrupt increases of solar wind velocity are found shortly before 00:00 and around 23:00 coordinated universal time (UTC) on 7 September, and the largest value exceeds 800 km/s around 07:00 UTC on 8 September. The data gap of  $V_{sw}$  around 11 September is due to a solar energetic proton event as reported by Redmon et al. (2018). The IMF components show large fluctuations when the solar wind is dynamic, and the southward  $B_z$  reaching minimum values of  $-31$  nT appears around 23:30 UTC on 7 September. An abrupt increase of the  $Sym-H$  index is seen around



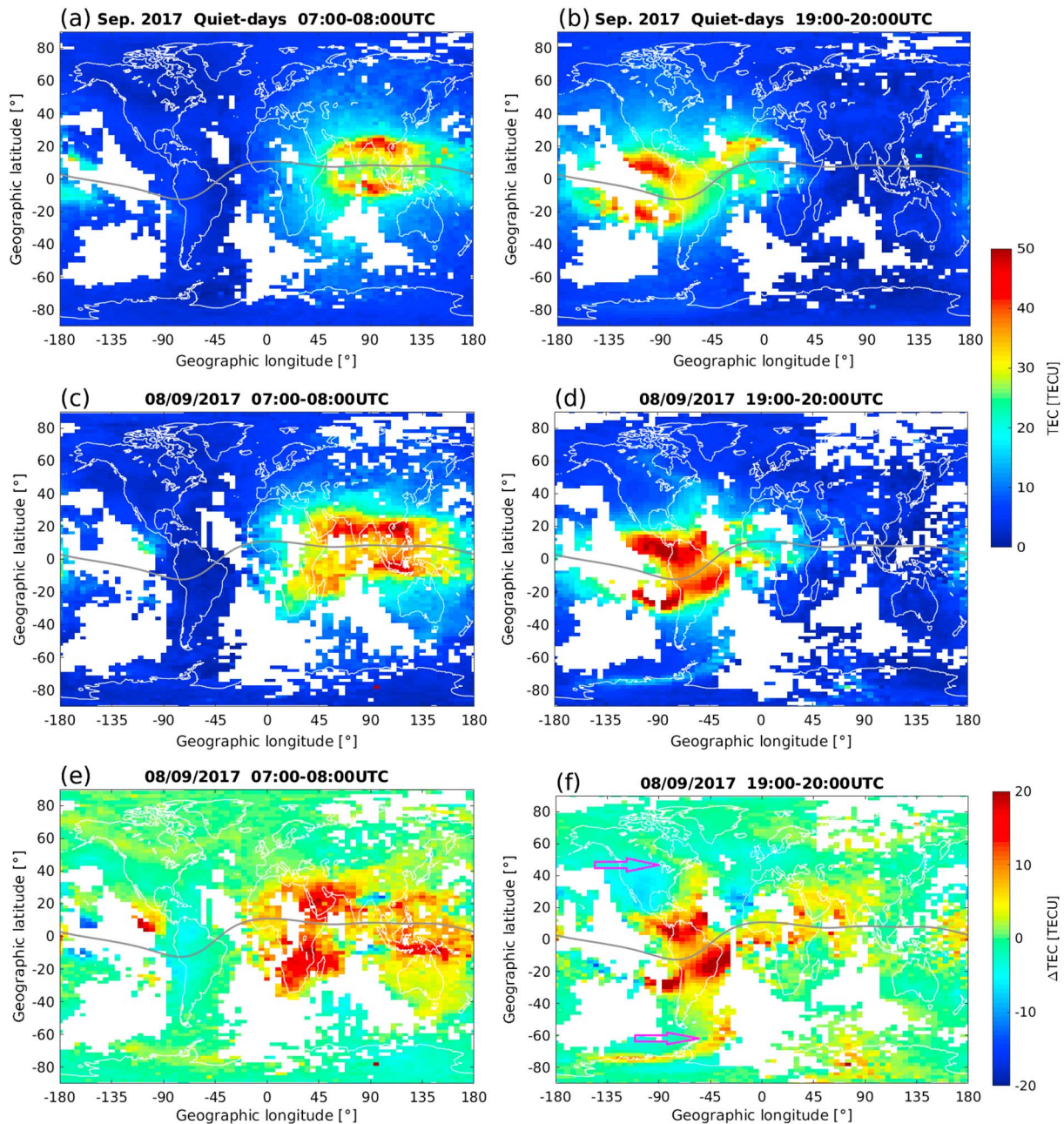


**Figure 2.** The global distribution of ground-based TEC during (a, b) magnetic quiet day and (c, d) beginning of storm recovery phase. Two 1-hr intervals are selected when the (left column) Asian and (right column) America longitudes are around noon hours. Panels e and f show the TEC perturbations ( $\Delta\text{TEC}$ ) during the beginning of storm recovery phase. TEC = total electron content.

23:40 UTC on 6 September indicating the sudden storm commencements concurrent with the jump in solar wind speed, and the peak  $\text{SYM-H}$  value of 46 nT appears 10 min later. A fast decrease of  $\text{SYM-H}$  is seen around midnight of 7 September, and the first minimum reaching  $-146$  nT appears around 01:10 UTC. A second minimum reaching  $-115$  nT appears around 14:00 UTC on 8 September. The two-step decrease of the  $\text{SYM-H}$  index (e.g., Kamide et al., 1998) on 8 September indicates that there are two major energy injections from the magnetosphere. Afterward, the  $\text{SYM-H}$  index gradually increases again, indicating the storm recovery phase. The global 3-hr  $K_p$  index reaches over 7 during the storm main phase and stays at levels less than 4 from 9 to 11 September; meanwhile, the  $V_{\text{SW}}$ ,  $B_z$ , and  $\text{SYM-H}$  also indicate quiet conditions during the recovery phase.

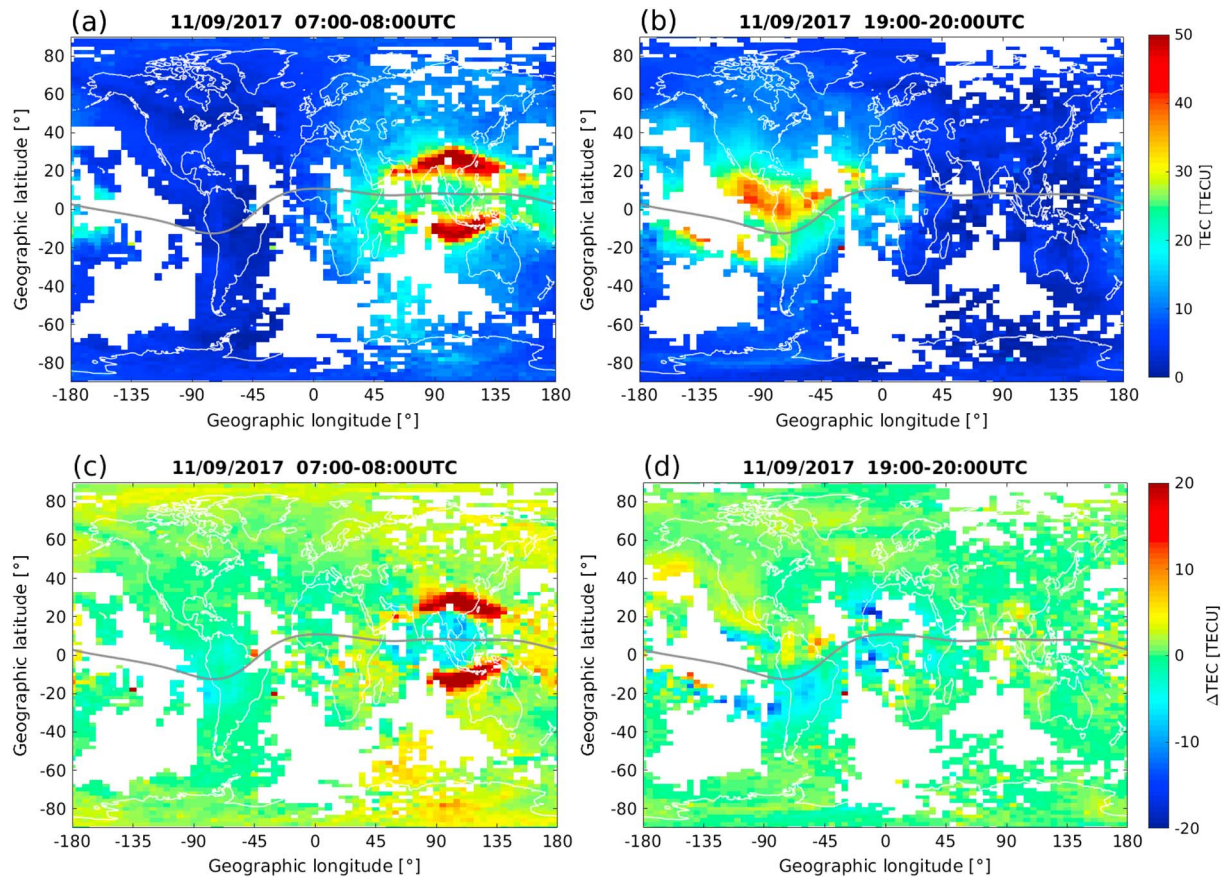


**Figure 3.** Same as Figure 2, but for the two 1-hr intervals of (a, b) TEC and (c, d) perturbation ( $\Delta$ TEC) on the storm recovery phase on 11 September 2017. TEC = total electron content.

### 3.2. Ground-Based TEC Measurements

Figures 2a and 2b present the global distributions of quiet-days averaged TEC during 07:00–08:00 and 19:00–20:00 UTC, when the Asian and American sectors are around local noon hours, respectively. Quiet days are selected from September 2017, for which the minimum *SYM-H* index of the day is not lower than  $-25$  nT and maximum value does not exceed 10 nT. The TEC values provided by the Madrigal database are sorted into bins of  $2^\circ \times 5^\circ$  (geographic latitude versus longitude), and the blank areas are due to lack of TEC data. The gray-solid line indicates the magnetic equator. From a global view the TEC shows larger value on the dayside than on the night side, and the crests of the ionospheric equatorial ionization anomaly (EIA) on the dayside extend to about  $\pm 15^\circ$  magnetic latitude (MLAT). The distributions of TEC during the same two 1-hr intervals (at the very beginning of the storm recovery phase) on 8 September are shown in Figures 2c and 2d. Compared to the quiet time pattern, the dayside TEC values are enhanced at low and equatorial latitudes in both the Asian and American sectors. When subtracting the quiet day reference, the dayside TEC enhancements at EIA crests exceed 20 TECU for both intervals. Around 07:00–08:00 UTC a TEC enhancement at the northern EIA crest around  $-120^\circ$ E is also evident; around 19:00–20:00 UTC, two enhanced TEC bands (indicated by magenta arrows) extending from high to middle latitudes are seen in the American sector (more prominent in the Southern Hemisphere; Figure 2f), which are possibly related to traveling ionospheric disturbances as reported by Aa et al. (2019).

Figure 3 shows the distributions of TEC, as well as the perturbations ( $\Delta$ TEC), during the same two 1-hr intervals but at the late storm recovery phase on 11 September 2017. During 07:00–08:00 UTC (Figure 3c), the daytime TECs at EIA crests of the Asian sector show clear enhancements larger than 40 TECU, which even exceed the enhancement shown in Figure 2e. However, during 19:00–20:00 UTC (Figure 3d), the daytime



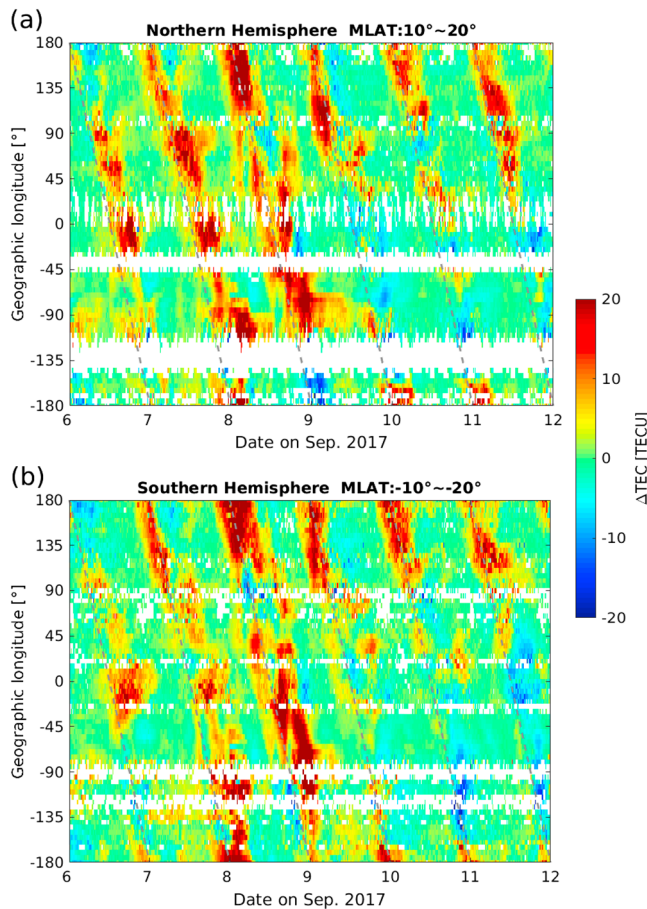


**Figure 4.** The longitude versus coordinated universal time (in a time cadence of 15 min) variations of TEC during 6–11 September 2017 for the (a) northern (10–20° MLAT) and (b) southern (–10° to –20° MLAT) equatorial ionization anomaly crest regions. The gray dashed lines represent the local noon at different longitudes. TEC = total electron content; MLAT = magnetic latitude.

TEC at EIA crests of the American and African sectors exhibit mainly negative perturbations, which is opposite to the pattern observed during the earlier storm recovery phase (Figure 2f).

To further check the TEC variations at EIA crest regions during the entire storm period, the TEC values are first assigned to their magnetic coordinates and then are sorted into bins of  $2^\circ \times 5^\circ$  (MLAT versus geographic longitude) with a time cadence of 15 min. The same approach has been applied to the quiet day TEC and then subtracted from the values of storm period. Figures 4a and 4b present the longitude versus UTC (with a time cadence of 15 min) variations of  $\Delta\text{TEC}$  during 6–11 September for the northern (10–20° MLAT) and southern (–10° to –20° MLAT) EIA crest regions, respectively. The gray dashed lines represent local noon at the different longitudes. In the northern EIA crest regions positive values of  $\Delta\text{TEC}$  are seen at almost all longitudes during the storm main phase on 7–8 September. However, from 9 September to the end of 11 September, daytime positive  $\Delta\text{TEC}$  is only evident at Asian longitudes, while it exhibits negative values at American longitudes. A similar longitudinal dependence of  $\Delta\text{TEC}$  is found for the southern EIA crest region, showing also opposite ionospheric responses at Asian and American longitudes during the storm recovery phase.

### 3.3. In Situ Electron Density Measurements from the Swarm Satellites

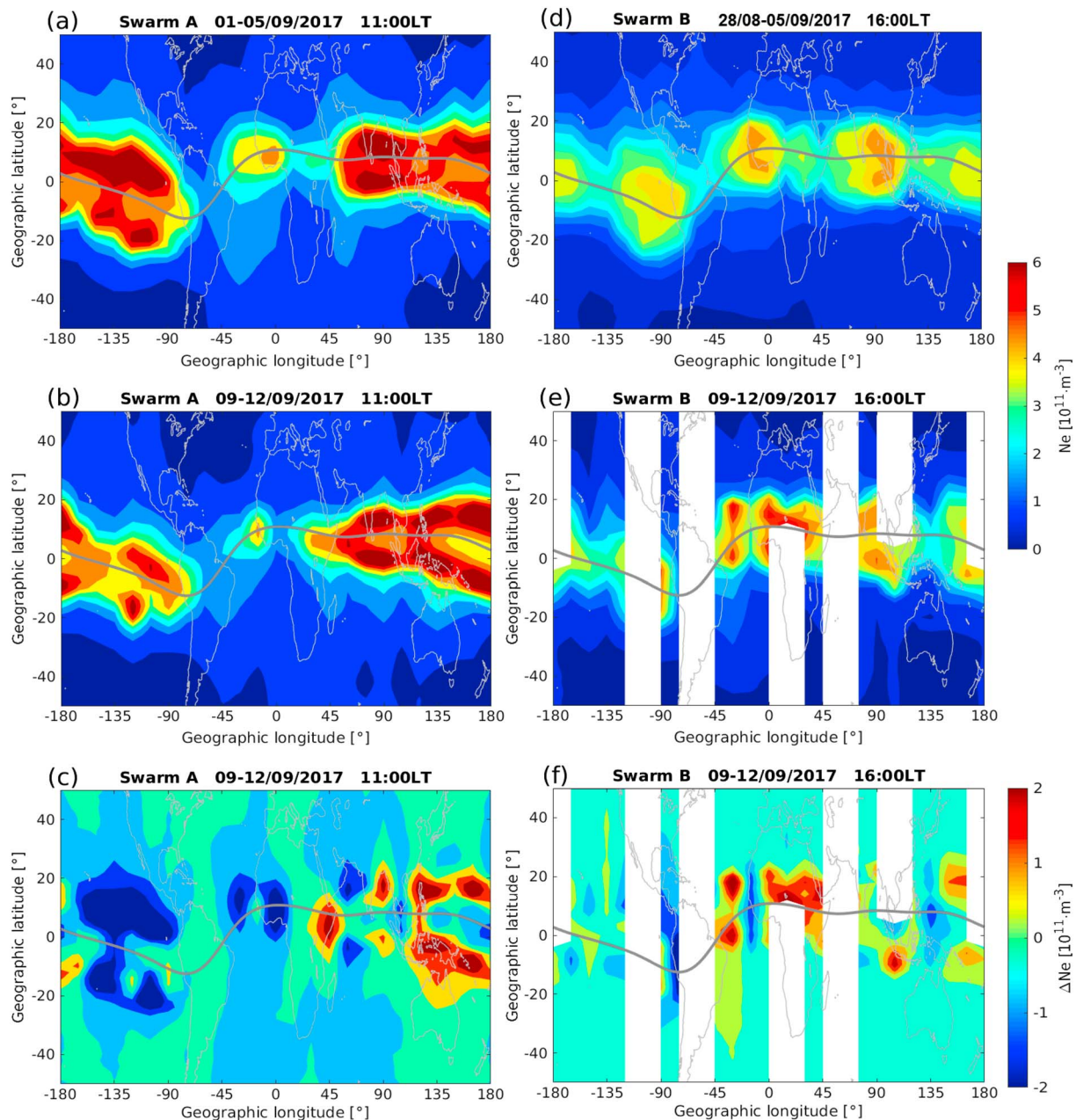
As a polar orbiting satellite, Swarm probes the ionosphere at almost constant LT over a couple of days. Therefore, it provides a good opportunity for checking the longitudinal variations of the ionosphere for a given LT.

Figure 5 shows the distributions of in situ electron density,  $N_e$ , from (left) Swarm A at about 450 km and (right) Swarm B at about 510 km, respectively. Here, we show only results from the dayside orbit arcs, which are around 11:00 and 16:00 LT for the two satellites, respectively. And the electron density readings are confined to the  $\pm 50^\circ$  geographic latitude range, to focus on equatorial and low latitudes. The magnetic equator is indicated by the gray solid lines. Clear longitudinal wave-4 patterns are seen during the prestorm period in observations of both satellites, which is mainly caused by the upward propagating nonmigrating tidal component DE3 from the lower atmosphere (e.g., Hagan & Forbes, 2002), as August–September is a favorable season for DE3 (e.g., Lühr et al., 2012; Oberheide et al., 2009). We want to note that the prestorm date of 1–5 September have been selected for Swarm A, while data from 28 August to 5 September used for Swarm B, as it needs a longer period to cover the same LT interval. By subtracting the pre-storm electron density distributions (panels a and d) from the values during the storm recovery phase (panels b and e), the  $N_e$  perturbations from Swarm A at 11:00 LT (panel c) show clear positive and negative values at Asian and American sectors, respectively, which is consistent with the ground-based TEC observations as shown in Figure 3. Due to the lack of electron density measurements by Swarm B on 11 September, we could not provide a complete global overview of  $\Delta N_e$  around 16:00 LT from Swarm B (panel f), but we still see that the EIA crests in the American sector exhibit mainly a negative perturbation, while they exhibit a positive perturbation at Asian longitudes.

## 4. Discussions

### 4.1. Comparison With the Opposite Longitudinal Response During the Storm Recovery Phase on 17–18 March 2015

Zhou et al. (2016) reported that the TEC perturbations during the recovery phase of the St. Patrick's Day storm 2015 showed also prominent longitudinally opposite variations (see their Figure 6). Therefore, we would like to check if such a longitude-dependent ionospheric response has similar characteristics as that observed in the September 2017 storm.



**Figure 5.** The global distribution of in situ electron density and perturbations from (a–c) Swarm A and (d–f) Swarm B satellites on the dayside.  $N_e$  at (a, d) prestorm days and (b, e) storm recovery phase as well as (c, f) their differences are shown for comparison.

Figure 6a provides an overview of the variations of solar wind velocity, IMF components, geomagnetic indices  $SYM-H$ , the 3-hr  $K_p$  on 16–21 March 2015. The IMF components show clearly fluctuations starting from 04:04 UTC on 17 March 2015. As a response, the sudden storm commencement is recorded by the  $SYM-H$  index with an amplitude of 67 nT at about 04:48 UTC. The global 3-hr  $K_p$  index exceeds 7 when the  $SYM-H$  index reaches its minimum value of  $-234$  nT. From 18 March, the IMF components and  $SYM-H$  start to recover back to their quiet time level but show significant fluctuations during the rest of days.

Figure 6b shows the global distribution of TEC perturbation ( $\Delta TEC$ ) between 04:00 and 05:00 UTC on 18 March 2015. The positive ionospheric responses at EIA crest regions are observed between  $-120^\circ\text{E}$  and  $60^\circ\text{E}$ , while at other longitudes it exhibits a prominent negative response. Interestingly, these longitudinally opposite ionospheric responses are drifting from east to west with UTC evolution, as shown in Figures 6c



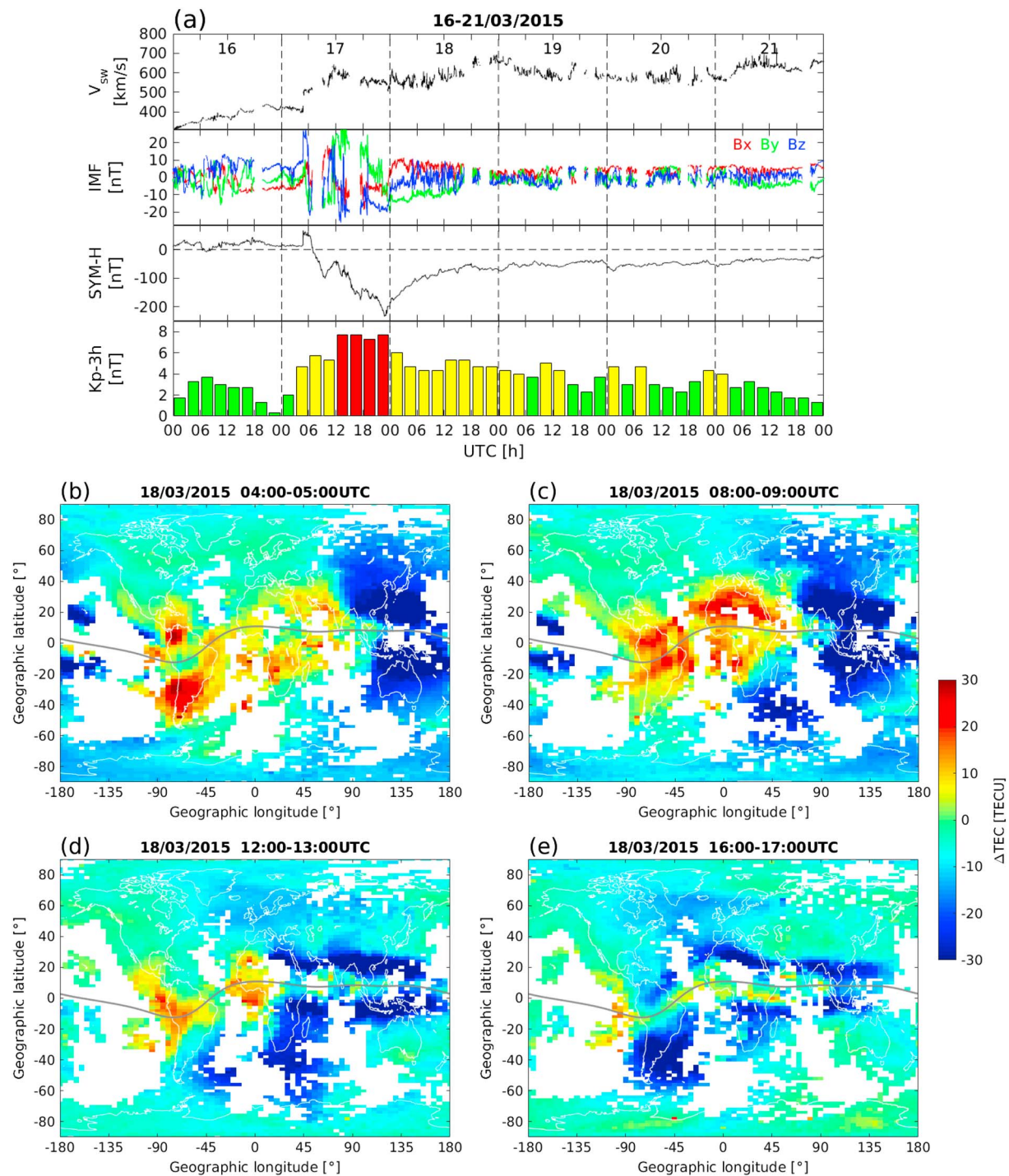


**Figure 6.** (a) The variations of solar wind velocity, IMF components, SYM-H index, and 3-hr Kp index on 16–21 March 2015. Panels (b)–(e) show the global distribution of TEC for different UTC hours on 18 March 2015. IMF = interplanetary magnetic field; TEC = total electron content; UTC = coordinated universal time.

and 6d. To see the TEC perturbations at EIA crest regions during the entire storm period, Figure 7 shows the longitude versus UTC variations of  $\Delta\text{TEC}$  during 16–21 March 2015 for the northern ( $10^{\circ}$ – $20^{\circ}$  MLAT) and southern ( $-10^{\circ}$  to  $-20^{\circ}$  MLAT) EIA crest regions, respectively. We see that  $\Delta\text{TEC}$  shows mainly negative values during the storm main phase, most prominent in the eastern hemisphere on 18 March. And the negative storm response is dominant only from noon to evening hours for all longitudes, while from

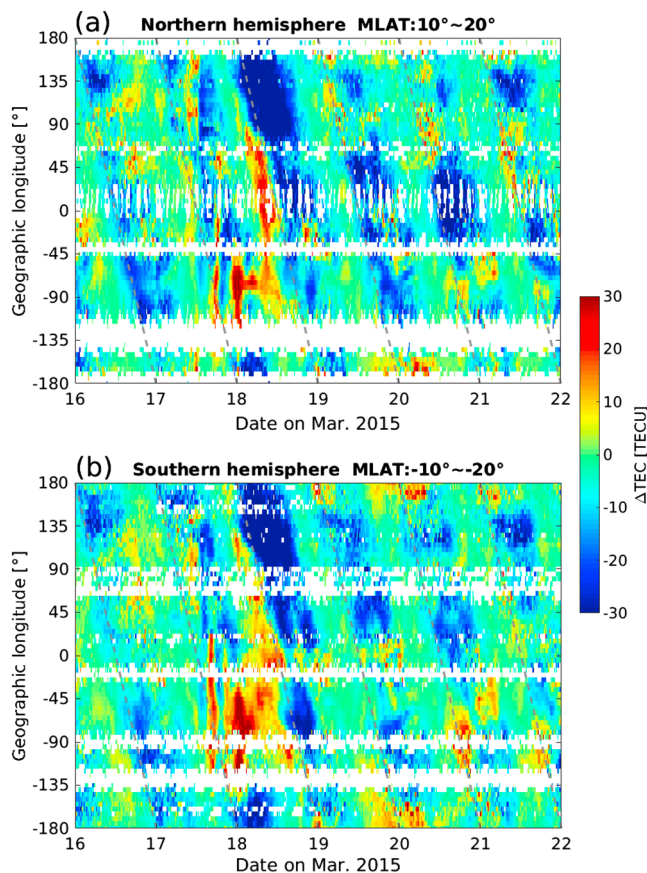


**Figure 7.** The longitude versus coordinated universal time (in a time cadence of 15 min) variations of TEC during 16–21 March 2015 for the (a) northern (10–20° MLAT) and (b) southern (–10° to –20° MLAT) equatorial ionization anomaly crest regions. The gray dashed lines represent the local noon at different longitudes. TEC = total electron content; MLAT = magnetic latitude.

morning to prenoon hours the ionosphere exhibits mainly a positive response. This feature repeats, although less prominent, during the rest of days in the storm recovery phase.

Such LT dependent ionospheric response can also be interpreted as an opposite longitudinal response, as it causes positive/negative  $\Delta\text{TEC}$  values within fixed but separated LT sectors. As suggested by Zhou et al. (2016), such positive ionospheric effect in the morning/prenoon sector, as well as the negative during afternoon/evening hours is possibly the combined effect of disturbance meridional wind and vertical plasma drift. Enhanced equatorward wind is pushing the ions up along the field lines during magnetically disturbed periods (Prölss, 1995), and the significant upward ion drift can also appear with the start of the recovery phase in the morning sector (Huang et al., 2016). These drivers are mainly fixed in LT. From this point of view, the opposite longitudinal response observed during the recovery phase on 17–18 March 2015 storm is indeed a storm-related LT effects. However, when looking back to the TEC perturbations during the recovery phase of the September 2017 storm, the longitudinally opposite response appears during daytime hours, and positive/negative TEC perturbations persist in the Asian/American sectors. Such a longitudinally opposite response of the ionosphere is different from that during the 17–18 March 2015 storm, which also suggests different drivers.

#### 4.2. Composition Changes or Electrodynamics

Astafyeva et al. (2015) explained that the different ionospheric responses in the American and European-African longitudinal sectors during the St. Patrick's Day storm 2015 main phase are caused by the longitude-dependent neutral composition changes. Therefore, we checked also the global distribution of  $\text{O}/\text{N}_2$  measured by GUVI on the TIMED satellite during 6–11 September 2017, and the result is shown in Figure 8. We want to point out that GUVI cannot provide a snapshot of the global  $\text{O}/\text{N}_2$  distribution at a given time, rather the result presented in each subpanels is derived by averaging the  $\text{O}/\text{N}_2$  values over the corresponding day. As revealed by Kil and Paxton (2011), the  $\text{O}/\text{N}_2$  ratio at EIA

regions is mainly accounted for by the 135.6-nm emission of radiative  $\text{O}^+$  recombination; therefore, the longitudinal pattern of  $\text{O}/\text{N}_2$  corresponds to the longitudinal pattern of EIA intensity. During this storm the TIMED satellite flew at around the 11:00 LT sector. On 6 September (before the storm), at low and middle latitudes the  $\text{O}/\text{N}_2$  shows larger values at Asian, African, and Pacific longitudes. The very large values (red spots) near South Africa and northern Asia are possibly due to outliers in the  $\text{O}/\text{N}_2$  estimation. At the storm main phase, on 7 September,  $\text{O}/\text{N}_2$  is enhanced at Atlantic and West African longitudes, but stronger enhancements are found at almost all the longitudes on 8 September. On 9 September enhanced  $\text{O}/\text{N}_2$  is only evident in the Asian sector, which indicates an enhanced EIA magnitude at this longitude. However, during the following two days the  $\text{O}/\text{N}_2$  ratio shows a clear longitudinal wave-4 pattern with comparable amplitudes at the wave-peak longitudes; therefore, the composition change can explain the TEC enhancement at the Asian sector on 9 September, but it cannot explain well the opposite ionospheric response in the Asian and American longitudes on 11 September as shown in our Figures 3 and 4.

Beside neutral composition changes, the PPEFs and DDEFs at storm periods are widely used for explaining the ionospheric responses at middle and low latitudes. During the early stage of storms, the PPEFs occur nearly simultaneously at all latitudes with timescales of about 1 hr (e.g., Fejer et al., 1983; Scherliess & Fejer, 1997). Conversely, setting up the DDEFs needs a couple of hours due to the inertia of the neutral air (e.g., Ritter et al., 2010; Xiong et al., 2015). As PPEF are commonly directed dawn to dusk, it mainly causes the dayside positive and nightside negative storm effects (e.g., Astafyeva, 2009;



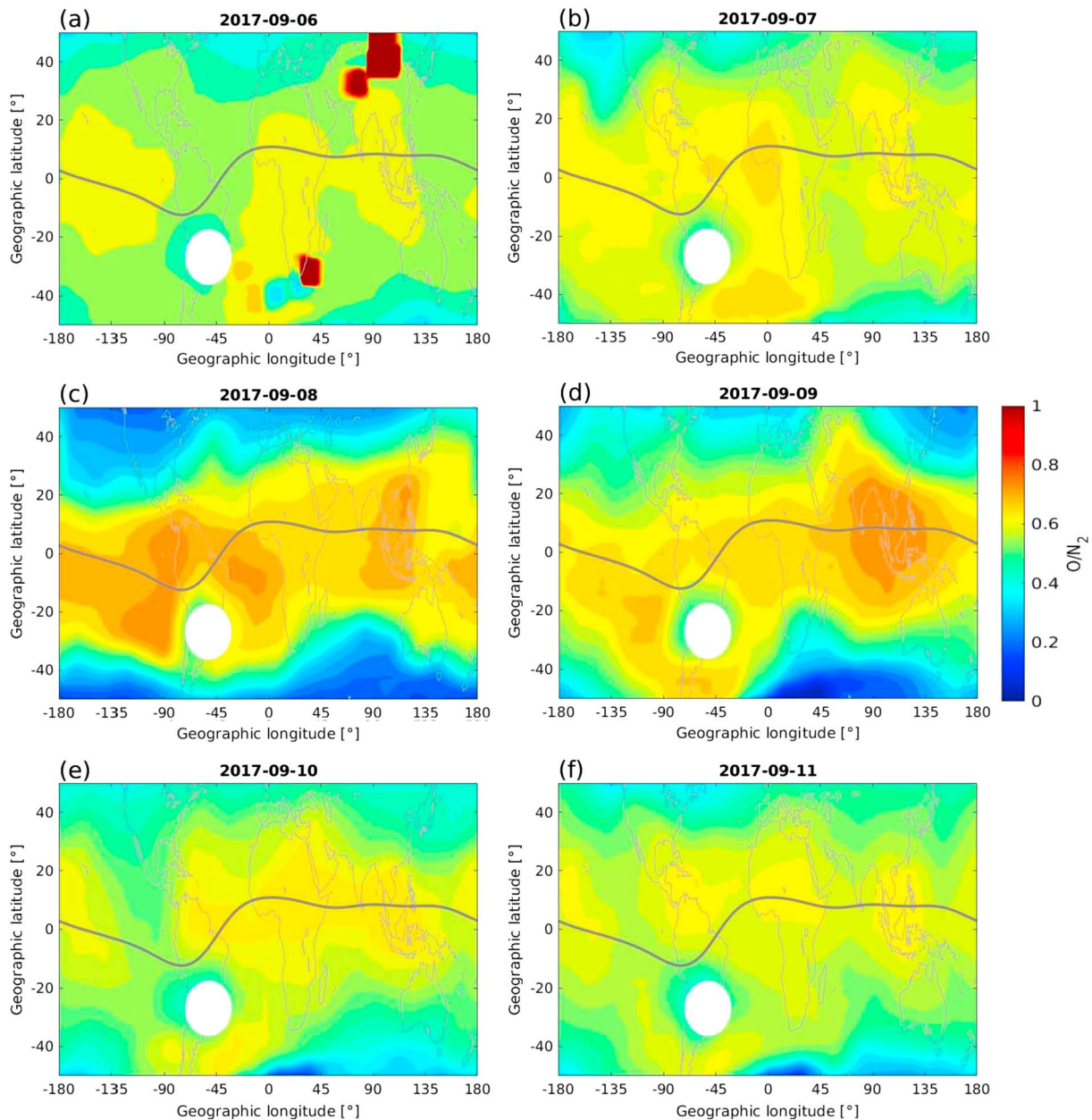


**Figure 8.** The global distribution of global ultraviolet imager measured O/N<sub>2</sub> ratio during (a–f) 6–11 September 2017.

Huang et al., 2005). Therefore, the PPEFs cannot explain the daytime TEC enhancements in the Asian sector during the storm recovery phase on 9–11 September 2017. The DDEFs can sometime last up to several days (e.g., Scherliess & Fejer, 1997; Yamazaki & Kosch, 2015); however, they are mainly directed westward on the dayside and should cause a decrease of plasma density (Tsurutani et al., 2004) but not an enhancement. Neutral winds in the ionospheric *E* region are important for changing the ionospheric currents and electric fields through a dynamo process (Heelis, 2004; Richmond, 1995), and the electric fields will intensify or reduce the ionospheric fountain via  $E \times B$  drift and modulate the TEC perturbations at equatorial and low-latitude regions. As shown by Lei et al. (2018), the eastward zonal wind at about 80–95 km in the Asian sector is strongly enhanced on 9–11 September 2017, which will further cause the enhancement of ionospheric *E* region currents and electric fields at Asian longitudes.



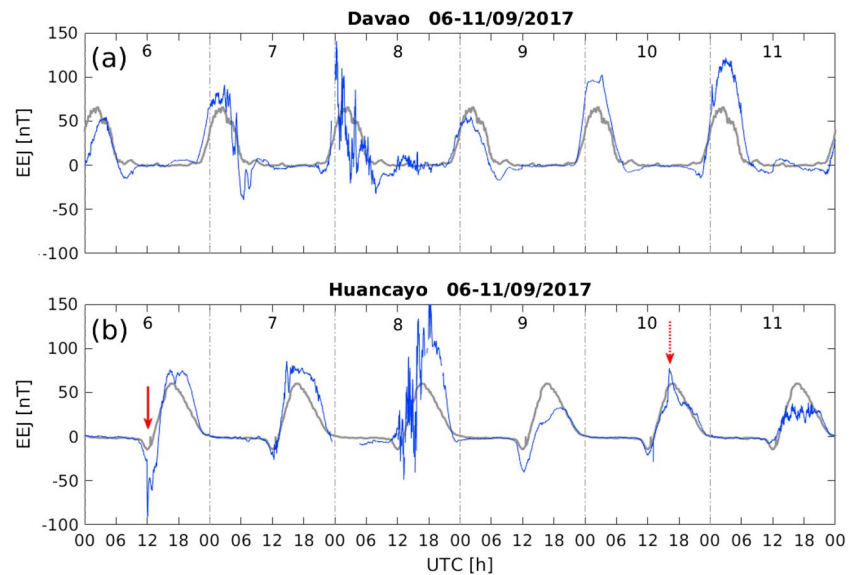


**Figure 9.** The EEJ variations at (a) Davao (Asia) and (b) Huancayo (America) on 6–11 September 2017. The gray lines represent the monthly quiet day reference, while the blue lines are the actual EEJ variations. Red arrows mark the effects of solar flares. EEJ = equatorial electrojet.

For checking the  $E$  region current variations in the American and Asian sectors, Figure 9 shows the EEJ variations at Davao (Asian) and Huancayo (America) on 6–11 September 2017. The gray lines represent the monthly quiet day reference, while the blue lines are the actual EEJ variations. Clear perturbations of the EEJ are seen at both stations during the storm main phase. The EEJ is increased by about 100% at Davao on 10–11 September, while it is reduced by about 50% at Huancayo on 9–11 September, which is consistent with the opposite TEC perturbations in the Asian and American sectors. It is worth pointing out that the EEJ peaks observed at Huancayo indicated by red arrows are caused by the X8.2 class solar flare peaking at 16:06 UTC on 10 September 2017 and by the X9.3 class solar flare peaking at 12:02 UTC on 6 September, which also largely enhances the EEJ but with a negative value (indicated by the red solid arrow), as the  $E$  region electric field points westward at early morning hours. The increased X-rays and extreme ultraviolet irradiance during a solar flare will enhance the Cowling conductivity and further modulate the equatorial ionospheric electrodynamics (e.g., Rastogi et al., 1997; Zhang et al., 2019). The opposite modifications of the EEJ at the two stations indicate that the opposite daytime ionospheric responses in the Asian and American sectors are more likely due to the modulation of the lower ionospheric electrodynamics.

#### 4.3. Possible Contributions of Planetary Waves and Tides From Below

Pedatella et al. (2008) found that the longitudinal variability in the ionosphere generated by atmospheric tides of tropospheric origin is briefly disrupted during the initial phase of a geomagnetic storm, due to the superposition of storm-related disturbances. But the tidal signature reappears during the recovery phase. This is also evident in our Figure 8 where clear longitudinal wave-4 patterns of  $O/N_2$  reappeared during the later storm recovery phase on 10–11 September 2017, but less obvious during the pre-storm and storm main phase on 6–8 September. Such a longitudinal wave-4 pattern of the ionosphere is commonly related to the effect of upward propagating nonmigrating tide DE3. If we assume the opposite response of the ionosphere in the Asian and American sectors to be an eastward propagating longitudinal wave-1 pattern, it can be interpreted as tidal forcing propagating upward from the lower atmosphere.

The planetary waves and nonmigrating tides both can cause longitudinal wave-1 patterns. The modulation by planetary waves can be described as (e.g., Yamazaki, 2018)

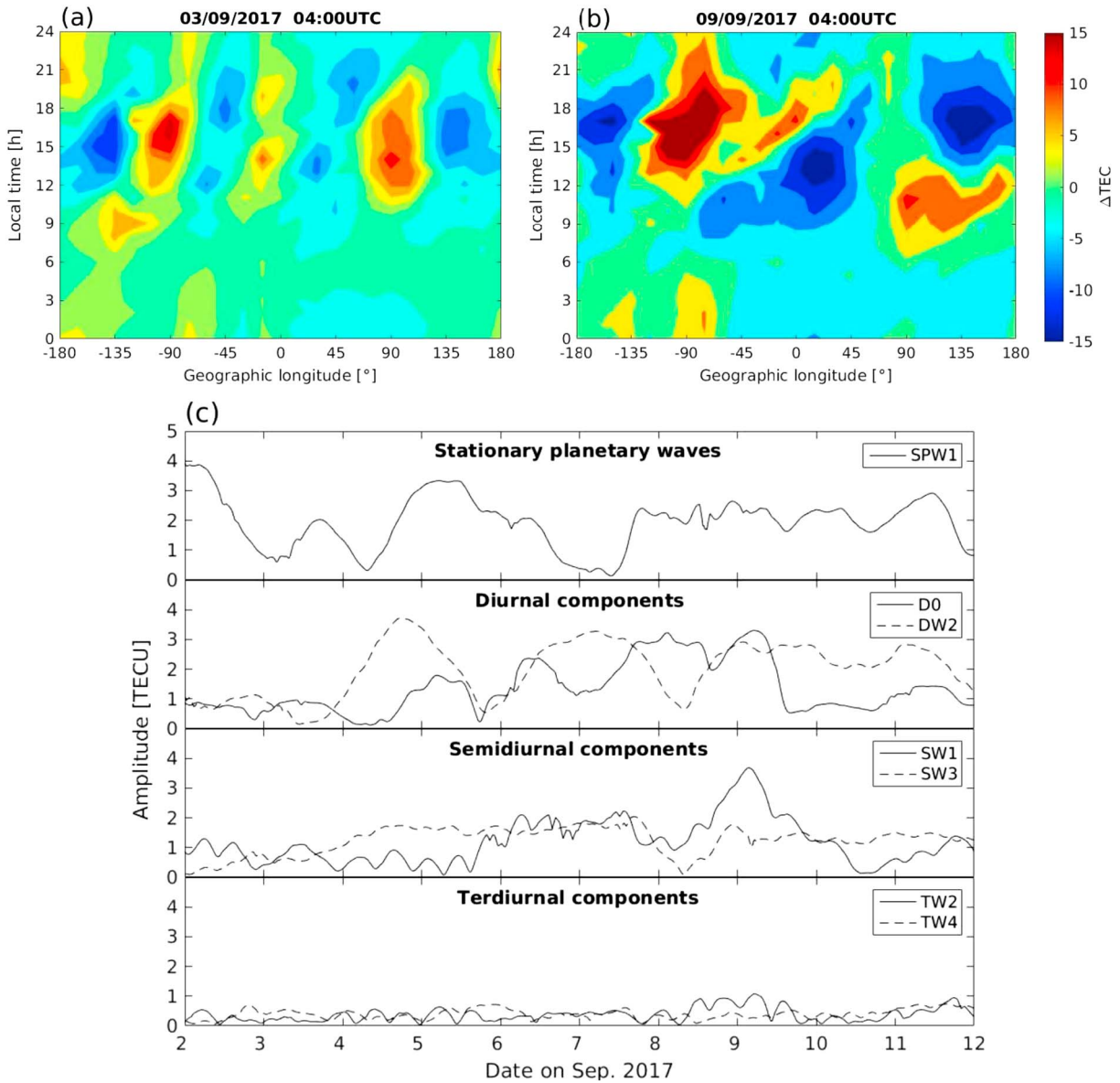


**Figure 10.** (a, b) The variations of nonmigrating tidal components that caused longitudinal wave-1 patterns during 2–11 September 2017. (c) The amplitudes are derived from the ground-based TEC measurements.

$$A \cos \left[ 2\pi \left( \frac{t}{T} + s \frac{\lambda}{360} - \phi \right) \right] \quad (1)$$

where  $A$  is the amplitude of the wave,  $t$  is the universal time (in days),  $T$  is the period of the wave (in days),  $s$  is the zonal wavenumber (for longitudinal wave-1 pattern,  $s = 1$ ),  $\lambda$  is the longitude (in degrees), and  $\phi$  is the phase of the wave. The planetary waves, for example, with periods of 6-, 10-, or 16-day, induced wave peaks will slowly move in longitudes with time. However, the westward phase shifts expected from these planetary waves are not seen in our Figure 4. Instead, the wave-1 peak persists at the Asian longitudes during 9–11 September, indicating it should not be caused by planetary waves.

In a next step, we check the components from the nonmigrating tide. As the nonmigrating tides are usually resolved in the LT versus longitudinal frame, the universal time  $t$  in equation (1) has been replaced by the LT,  $t_{\text{LT}}$ . The modulation of nonmigrating tides, as observed by satellites, is defined as (e.g., Häusler & Lühr, 2009)

$$A_{n,s} \cos \left[ 2\pi \left( n\Omega t_{LT} + (s-n) \frac{\lambda}{360} - \phi_{n,s} \right) \right] \quad (2)$$

where  $A_{n,s}$  is amplitude,  $n$  denotes a harmonic of a solar day,  $\Omega$  is the rotation rate of the Earth,  $t_{LT}$  is the LT,  $s$  is again the zonal wavenumber, and  $\phi_{n,s}$  is the phase of the tidal component. The tidal signatures with  $|s - n| = 1$  will result in longitudinal wave-1 patterns. Examples for that are the stationary planetary wave SPW1 ( $n = 0, s = 1$ ), diurnal components D0 ( $n = 1, s = 0$ ) and DW2 ( $n = 1, s = 2$ ), semidiurnal components SW1 ( $n = 2, s = 1$ ), and SW3 ( $n = 2, s = 3$ ), as well as terdiurnal components TW2 ( $n = 3, s = 2$ ) and TW4 ( $n = 3, s = 4$ ). The letters E or W denote tides propagating eastward or westward.

To determine the contributions of these nonmigrating tides, a least squares fit of equation (2) has been applied to the TEC measurements. To focus on the EIA crest regions, only the TEC data within  $\pm 10$ – $20^\circ$  MLAT have been considered, and a sliding window of 24 UTC hours has been used to get the full LT coverage at all longitudes. A similar approach has been used by Xiong et al. (2014) for resolving the seasonal and latitudinal variations of nonmigrating tidal components in the ionosphere, and readers are suggest to referring to it. Figures 10a and 10b show the LT versus longitude variation of  $\Delta$ TEC around 04:00 UTC on 3 and 9 September, respectively. Here,  $\Delta$ TEC means the longitudinal mean value has been subtracted for each LT (e.g., Xiong et al., 2014). Before the storm on 3 September  $\Delta$ TEC shows clear longitudinal wave-4 patterns at daytime. But during the earlier recovery phase on 9 September,  $\Delta$ TEC shows mainly a longitudinal wave-1 pattern, and the wave peak changes around noon from maximum in the Asian to minimum in the African-American sectors, indicating an effect of the semidiurnal tidal component SW1 (as will be confirmed below).

Figure 10c shows the estimated time variations of the tidal components that cause longitudinal wave-1 patterns during 2–11 September 2017. Before the storm the stationary planetary wave, SPW1, has the largest amplitude, and it is reduced somehow during the storm recovery phase. The diurnal components, D0 and DW2, show increased amplitudes starting from 4 and 5 September (before the storm), and the enhanced amplitudes of both tides persist through the storm main phase. However, D0 reduces its amplitude after 9 September while DW2 keeps almost the same amplitude until the end of 11 September. For the semidiurnal component, a prominent increase is seen in the amplitude of SW1 on 9 September. No prominent enhancements result for the two terdiurnal components.

The result shown in Figure 10 suggests that the diurnal tidal components, D0 and DW2 are already enhanced before the storm and persist through the storm main and earlier recovery phase. In addition, the semidiurnal component, SW1, is also enhanced during the early storm recovery phase. It might, together with D0, be the major tidal force that contributes to the opposite response of the ionosphere at Asian and American sectors on 9–11 September 2017. Further observational and simulation studies are need for addressing why and how these tides are enhanced, and if their enhancements are still related to the geomagnetic disturbances.

## 5. Summary

In this study, we focus on the opposite response of the low-latitude ionosphere at the Asian and American sectors during the storm recovery phase on 9–11 September 2017, and the main findings are summarized as follows:

1. The ground-based TEC as well as the  $F$  region in situ electron density observed by Swarm satellites show an interesting feature on the dayside, that the ionosphere exhibits a locally fixed prominent positive and negative response in the Asian and American longitudes, respectively.
2. This Asian/American longitudinal asymmetry of ionospheric response at storm recovery phase cannot be well explained by storm-induced neutral composition ( $O/N_2$ ) changes.
3. The comparison between the EEJ variations at Davao and Huancayo suggests that opposite ionospheric responses in the Asian and American longitudes should be closely associated with the interplay of  $E$  region electrodynamics.
4. By applying nonmigrating tidal analysis to the ground-based TEC data, we find the diurnal components, D0 and DW2, as well as semidiurnal component SW1 are clearly enhanced from prestorm to early recovery phase. Atmospheric tidal driving is suggested to be the main contributor to the opposite response of



the low-latitude ionosphere in the Asian and American longitudes during the recovery phase of September 2017 storm.

### Acknowledgments

The solar wind and IMF data are derived from the NASA's ACE mission, and they can be downloaded at the website of <http://www.srl.caltech.edu/ACE/ASC/level2/> website. The SYM-H data are provided by the world data center for geomagnetism, Kyoto (<http://wdc.kugi.kyoto-u.ac.jp/aeasy/index.html>). The 3-hr Kp index is derived from the GFZ German Research Centre for Geosciences (<https://www.gfz-potsdam.de/en/kp-index/>). The European Space Agency (ESA) is also acknowledged for providing the Swarm data (<http://earth.esa.int/swarm/>). GPS TEC data products and access through the Madrigal distributed data system (<http://cedar.openmadrigal.org/ftp/>) are provided to the community by the Massachusetts Institute of Technology under support from U.S. National Science Foundation Grant AGS-1762141. Data for TEC processing are provided from the following organizations: UNAVCO; Scripps Orbit and Permanent Array Center; Institut Geographique National, France; International GNSS Service; The Crustal Dynamics Data Information System (CDDIS); National Geodetic Survey; Instituto Brasileiro de Geografia e Estatística; RAMSAC CORS of Instituto Geográfico Nacional de la República Argentina; Arecibo Observatory; Low-Latitude Ionospheric Sensor Network (LISN); Topcon Positioning Systems, Inc.; Canadian High Arctic Ionospheric Network; Institute of Geology and Geophysics, Chinese Academy of Sciences, China Meteorology Administration; Centro di Ricerche Sismologiche; Système d'Observation du Niveau des Eaux Littorales (SONEL); RENAG: Réseau National GPS permanent; GeoNet, the official source of geological hazard information for New Zealand; GNSS Reference Networks; Finnish Meteorological Institute; and SWEPOS-Sweden. The EEJ results presented in this paper rely on the data collected at Huancayo. We thank Instituto Geofísico del Perú, for supporting its operation and INTERMAGNET for promoting high standards of magnetic observatory practice ([www.intermagnet.org](http://www.intermagnet.org)). We also thank the German Research Centre for Geosciences (GFZ) and Universidad Mayor de San Andrés (UMSA) for the operation of the magnetometer at Villa Remedios. The magnetometer data from Villa Remedios used in this study will be made available upon request. The authors thank E. Yizengaw, E. Zesta, M. B. Moldwin, and the rest of the AMBER and SAMBA team for the data. AMBER is operated by Boston College and funded by NASA and

### References

- Aa, E., Zou, S., Ridley, A., Zhang, S., Coster, A. J., Erickson, P. J., et al. (2019). Merging of storm time midlatitude traveling ionospheric disturbances and equatorial plasma bubbles. *Space Weather*, 17, 285–298. <https://doi.org/10.1029/2018SW002101>
- Astafeyeva, E., Zakharenkova, I., & Doornbos, E. (2015). Opposite hemispheric asymmetries during the ionospheric storm of 29–31 August 2004. *Journal of Geophysical Research: Space Physics*, 120, 697–714. <https://doi.org/10.1002/2014JA020710>
- Astafeyeva, E., Zakharenkova, I., & Förster, M. (2015). Ionospheric response to the 2015 St. Patrick's Day storm: A global multi-instrumental overview. *Journal of Geophysical Research: Space Physics*, 120, 9023–9037. <https://doi.org/10.1002/2015JA021629>
- Astafeyeva, E. I. (2009). Dayside ionospheric uplift during strong geomagnetic storms as detected by the CHAMP, SAC-C, TOPEX and Jason-1 satellites. *Advances in Space Research*, 43(11), 1749–1756. <https://doi.org/10.1016/j.asr.2008.09.036>
- Blanc, M., & Richmond, A. D. (1980). The ionospheric disturbance dynamo. *Journal of Geophysical Research*, 85, 1669–1686. <https://doi.org/10.1029/JA085iA04p01669>
- Christensen, A. B., Paxton, L. J., Avery, S., Craven, J., Crowley, G., Humm, D. C., et al. (2003). Initial observations with the Global Ultraviolet Imager (GUVI) in the NASATIMED satellite mission. *Journal of Geophysical Research*, 108(A12), 1451. <https://doi.org/10.1029/2003JA009918>
- Coster, A. J., Foster, J. C., & Erickson, P. J. (2003). Monitoring the ionosphere with GPS. *GPS World*, 14(5), 42–45.
- Emmert, J. T., Fejer, B. G., Shepherd, G. G., & Solheim, B. H. (2004). Average nighttime F region disturbance neutral winds measured by UARS WINDII: Initial results. *Geophysical Research Letters*, 31, L22807. <https://doi.org/10.1029/2004GL021611>
- Fejer, B. G., Jensen, J. W., & Su, S.-Y. (2008). Seasonal and longitudinal dependence of equatorial disturbance vertical plasma drifts. *Geophysical Research Letters*, 35, L20106. <https://doi.org/10.1029/2008GL035584>
- Fejer, B. G., Larsen, M. F., & Farley, D. T. (1983). Equatorial disturbance dynamo electric fields. *Geophysical Research Letters*, 10(7), 537–540. <https://doi.org/10.1029/GL010i007p00537>
- Fuller-Rowell, T. J., Codrescu, M. V., Roble, R. G., & Richmond, A. D. (1997). How does the thermosphere and ionosphere react to a geomagnetic storm? In B. T. Tsurutani, et al. (Eds.), *Magnetic Storms, Geo-phys. Monogr. Set*, (Vol. 98, pp. 203–225). Washington, DC: AGU.
- Goncharenko, L. P., Foster, J. C., Coster, A. J., Huang, C., Aponte, N., & Paxton, L. J. (2007). Observations of a positive storm phase on September 10, 2005. *Journal of Atmospheric and Solar - Terrestrial Physics*, 69(10–11), 1253–1272. <https://doi.org/10.1016/j.jastp.2006.09.011>
- Gonzalez, W. D., Joselyn, J. A., Kamide, Y., Kroehl, H. W., Rostoker, G., Tsurutani, B. T., & Vasyliunas, V. M. (1994). What is a geomagnetic storm? *Journal of Geophysical Research*, 99(A4), 5771–5792. <https://doi.org/10.1029/93JA02867>
- Hagan, M. E., & Forbes, J. M. (2002). Migrating and nonmigrating diurnal tides in the middle and upper atmosphere excited by tropospheric latent heat release. *Journal of Geophysical Research*, 107(D24), D244754. <https://doi.org/10.1029/2001JD001236>
- Häusler, K., & Lühr, H. (2009). Nonmigrating tidal signals in the upper thermospheric zonal wind at equatorial latitudes as observed by CHAMP. *Annales Geophysicae*, 27(7), 2643–2652. <https://doi.org/10.5194/angeo-27-2643-2009>
- Heelis, R. A. (2004). Electrodynamics in the low and middle latitude ionosphere: A tutorial. *Journal of Atmospheric and Solar-Terrestrial Physics*, 66(10), 825–838. <https://doi.org/10.1016/j.jastp.2004.01.034>
- Hocke, K., & Schlegel, K. (1996). A review of atmospheric gravity waves and traveling ionospheric disturbances: 1982–1995. *Annales Geophysicae*, 14(9), 917–940. <https://doi.org/10.1007/s00585-996-0917-6>
- Huang, C.-S., Foster, J. C., Goncharenko, L. P., Erickson, P. J., & Rideout, W. (2005). A strong positive phase of ionospheric storms observed by the Millstone Hill incoherent scatter radar and global GPS network. *Journal of Geophysical Research*, 110, A06303. <https://doi.org/10.1029/2004JA010865>
- Huang, C.-S., Wilson, G. R., Hairstone, M. R., Zhang, Y., Wang, W., & Liu, J. (2016). Equatorial ionospheric plasma drifts and O concentration enhancements associated with disturbance dynamo during the 2015 St. Patrick's Day magnetic storm. *Journal of Geophysical Research: Space Physics*, 121, 7961–7973. <https://doi.org/10.1029/2016JA023072>
- Huang, Y., Richmond, A. D., Deng, Y., & Roble, R. (2012). Height distribution of Joule heating and its influence on the thermosphere. *Journal of Geophysical Research*, 117, A08334. <https://doi.org/10.1029/2012JA017885>
- Kamide, Y., Yokoyama, N., Gonzalez, W. D., Tsurutani, W. D., Brekke, A., & Masuda, S. (1998). Two-step development of geomagnetic storms. *Journal of Geophysical Research*, 103(A4), 6917–6921. <https://doi.org/10.1029/97JA03337>
- Kelley, M. C., Makela, J. J., Chau, J. L., & Nicolls, M. J. (2003). Penetration of the solar wind electric field into the magnetosphere/ionosphere system. *Geophysical Research Letters*, 30(4), 1158. <https://doi.org/10.1029/2002GL016321>
- Kikuchi, T., Lühr, H., Kitamura, T., Saka, O., & Schlegel, K. (1996). Direct penetration of the polar electric field to the equator during a DP 2 event as detected by the auroral and equatorial magnetometer chains and the EISCAT radar. *Journal of Geophysical Research*, 101, 17,161–17,173. <https://doi.org/10.1029/96JA01299>
- Kil, H., & Paxton, L. J. (2011). The origin of the nonmigrating tidal structure in the column number density ratio of atomic oxygen to molecular nitrogen. *Geophysical Research Letters*, 38, L19108. <https://doi.org/10.1029/2011GL049432>
- Lei, J., Huang, F., Chen, X., Zhong, J., Ren, D., Wang, W., et al. (2018). Was magnetic storm the only driver of the long-duration enhancements of daytime total electron content in the Asian-Australian sector between 7 and 12 September 2017? *Journal of Geophysical Research: Space Physics*, 123, 3217–3232. <https://doi.org/10.1029/2017JA025166>
- Lühr, H., Rother, M., Häusler, K., Fejer, B., & Alken, P. (2012). Direct comparison of non-migrating tidal signatures in the electrojet, vertical plasma drift and equatorial ionization anomaly. *Journal of Atmospheric and Solar - Terrestrial Physics*, 75–76, 31–43. <https://doi.org/10.1016/j.jastp.2011.07.009>
- Nishida, A. (1968). Coherence of geomagnetic DP 2 fluctuations with interplanetary magnetic variations. *Journal of Geophysical Research*, 73, 5549–5559. <https://doi.org/10.1029/JA073i017p05549>
- Oberheide, J., Forbes, J. M., Häusler, K., Wu, Q., & Bruinsma, S. L. (2009). Tropospheric tides from 80 to 400 km: Propagation, inter-annual variability, and solar cycle effects. *Journal of Geophysical Research*, 114, D00I05. <https://doi.org/10.1029/2009JD012388>
- Pedatella, N. M., Forbes, J. M., Lei, J., Thayer, J. P., & Larson, K. M. (2008). Changes in the longitudinal structure of the low-latitude ionosphere during the July 2004 sequence of geomagnetic storms. *Journal of Geophysical Research*, 113, A11315. <https://doi.org/10.1029/2008JA013539>

AFOSR. The authors thank Yaqi Jin for his fruitful discussion. Chao Xiong is partly supported by the project STO 1074/3-2 of the Priority Program 1788 "Dynamic Earth" funded by the German Research Foundation.

- Pedatella, N. M., & Liu, H. -L. (2018). The influence of internal atmospheric variability on the ionosphere response to a geo-magnetic storm. *Geophysical Research Letters*, 45, 4578–4585. <https://doi.org/10.1029/2018GL077867>
- Pröls, G. (1995). Ionospheric *F*-region storms. In H. Volland (Ed.), *Handbook of Atmospheric Electrodynamics* (Vol. 2, pp. 195–248). Boca Raton, Fla: CRC Press.
- Pröls, G. W. (1993). On explaining the local time variation of ionospheric storm effects. *Annales Geophysicae*, 11, 19.
- Rastogi, R. G., Rao, D. R. K., Alex, S., Pathan, B. M., & Sastry, T. S. (1997). An intense SFE and SSC event in geomagnetic H, Y and Z fields at the Indian chain of observatories. *Annales Geophysicae*, 15(10), 1301–1308. <https://doi.org/10.1007/s00585-997-1301-x>
- Redmon, Robert, Daniel Seaton, Robert Steenburgh, Jing He, Juan Rodriguez (2018), September 2017's geoeffective space weather and impacts to Caribbean radio communications during hurricane response, Earth and Space Science Open Archive. <https://doi.org/10.1002/essoar.a530e85443c2d357.102532a29f074aec.2>
- Richmond, A. D. (1995). The ionospheric wind dynamo: Effects of its coupling with different atmospheric regions. In R. M. Johnson & T. L. Killeen (Eds.), *The upper mesosphere and lower thermosphere: A review of experiment and theory, Geophysical Monograph Series*, (Vol. 87, pp. 49–65). Washington, DC: American Geophysical Union.
- Richmond, A. D., & Matsushita, S. (1975). Thermospheric response to a magnetic substorm. *Journal of Geophysical Research*, 80, 2839–2850. <https://doi.org/10.1029/JA080i019p02839>
- Ritter, P., Lühr, H., & Doornbos, E. (2010). Substorm-related thermospheric density and wind disturbances derived from CHAMP observations. *Annales Geophysicae*, 28(6), 1207–1220. <https://doi.org/10.5194/angeo-28-1207-2010>
- Scherliess, L., & Fejer, B. G. (1997). Storm time dependence of equatorial disturbance dynamo zonal electric fields. *Journal of Geophysical Research*, 102(A11), 24,037–24,046. <https://doi.org/10.1029/97JA02165>
- Soares, G., Yamazaki, Y., Matzka, J., Pinheiro, K., Morschhauser, A., Stolle, C., & Alken, P. (2018). Equatorial counter electrojet longitudinal and seasonal variability in the American sector. *Journal of Geophysical Research: Space Physics*, 123, 9906–9920. <https://doi.org/10.1029/2018JA025968>
- Tsurutani, B., Mannucci, A., Iijima, B., Abdu, M. A., Sobral, J. H. A., Gonzalez, W., et al. (2004). Global dayside ionospheric uplift and enhancement associated with interplanetary electric fields. *Journal of Geophysical Research*, 109, A08302. <https://doi.org/10.1029/2003JA010342>
- Xiong, C., Lühr, H., & Fejer, B. G. (2015). Global features of the disturbance winds during storm time deduced from CHAMP observations. *Journal of Geophysical Research: Space Physics*, 120, 5137–5150. <https://doi.org/10.1002/2015JA021302>
- Xiong, C., Lühr, H., & Fejer, B. G. (2016). The response of equatorial electrojet, vertical plasma drift, and thermospheric zonal wind to enhanced solar wind input. *Journal of Geophysical Research: Space Physics*, 121, 5653–5663. <https://doi.org/10.1002/2015JA022133>
- Xiong, C., Lühr, H., & Stolle, C. (2014). Seasonal and latitudinal variations of the electron density nonmigrating tidal spectrum in the topside ionospheric *F* region as resolved from CHAMP observations. *Journal of Geophysical Research: Space Physics*, 119, 10,416–10,425. <https://doi.org/10.1002/2014JA020354>
- Yamazaki, Y. (2018). Quasi-6-day wave effects on the equatorial ionization anomaly over a solar cycle. *Journal of Geophysical Research: Space Physics*, 123, 9881–9892. <https://doi.org/10.1029/2018JA026014>
- Yamazaki, Y., & Kosch, M. J. (2015). The equatorial electrojet during geomagnetic storms and substorms. *Journal of Geophysical Research: Space Physics*, 120, 2276–2287. <https://doi.org/10.1002/2014JA020773>
- Yizengaw, E., & Moldwin, M. B. (2009). African Meridian B-field Education and Research (AMBER) Array. *Earth, Moon and Planets*, 104(1), 237–246. <https://doi.org/10.1007/s11038-008-9287-2>
- Yue, X., Wang, W., Lei, J., Burns, A., Zhang, Y., Wan, W., et al. (2016). Long-lasting negative ionospheric storm effects in low and middle latitudes during the recovery phase of the 17 March 2013 geomagnetic storm. *Journal of Geophysical Research: Space Physics*, 121, 9234–9249. <https://doi.org/10.1002/2016JA022984>
- Zhang, R., Liu, L., Le, H., & Chen, Y. (2019). Equatorial ionospheric electrodynamics over Jicamarca during the 6–11 September 2017 space weather event. *Journal of Geophysical Research: Space Physics*, 124, 1292–1306. <https://doi.org/10.1029/2018JA026295>
- Zhou, Y.-L., Lühr, H., Xiong, C., & Pfaff, R. F. (2016). Ionospheric storm effects and equatorial plasma irregularities during the 17–18 March 2015 event. *Journal of Geophysical Research: Space Physics*, 121, 9146–9163. <https://doi.org/10.1002/2016JA023122>